Publication Year	2017
Acceptance in OA@INAF	2020-08-27T12:46:47Z
Title	CMB-induced radio quenching of high-redshift jetted AGNs with highly magnetic hotspots
Authors	Wu, Jianfeng; GHISELLINI, Gabriele; Hodges-Kluck, Edmund; Gallo, Elena; Ciardi, Benedetta; et al.
DOI	10.1093/mnras/stx416
Handle	http://hdl.handle.net/20.500.12386/26880
Journal	MONTHLY NOTICES OF THE ROYAL ASTRONOMICAL SOCIETY
Number	468

Monthly Notices of the ROYAL ASTRONOMICAL SOCIETY

MNRAS **468,** 109–121 (2017)
Advance Access publication 2017 February 20

doi:10.1093/mnras/stx416

CMB-induced radio quenching of high-redshift jetted AGNs with highly magnetic hotspots

Jianfeng Wu,[1★] Gabriele Ghisellini,[2] Edmund Hodges-Kluck,[1] Elena Gallo,[1] Benedetta Ciardi,[3] Francesco Haardt,[4,5] Tullia Sbarrato[6] and Fabrizio Tavecchio[2]

[1]*Department of Astronomy, University of Michigan, 1085 S University Ave, Ann Arbor, MI 48109, USA*
[2]*INAF – Osservatorio Astronomico di Brera, Via Bianchi 46, I-23807 Merate, Italy*
[3]*Max Planck Institute for Astrophysics, Karl-Schwarzschild Strasse 1, D-85741 Garching, Germany*
[4]*DiSAT, Università dell'Insubria, via Valleggio 11, I-22100 Como, Italy*
[5]*INFN, Sezione di Milano-Bicocca, Piazza della Scienza 3, I-20126 Milano, Italy*
[6]*Dipartimento di Fisica 'G. Occhialini', Università di Milano-Bicocca, Piazza della Scienza 3, I-20126 Milano, Italy*

Accepted 2017 February 15. Received 2017 February 14; in original form 2016 October 21

ABSTRACT

In an effort to understand the cause of the apparent depletion in the number density of radio-loud active galactic nuclei (AGNs) at $z > 3$, this work investigates the viability of the so-called cosmic microwave background (CMB) quenching mechanism of intrinsically jetted, high-z AGNs, whereby inverse Compton scattering of CMB photons off electrons within the extended lobes results in a substantial dimming of the lobe synchrotron emission at GHz frequencies, while simultaneously boosting their diffuse X-ray signal. We focus on five $z > 3.5$ radio galaxies that have sufficiently deep *Chandra* exposure (>50 ks) to warrant a meaningful investigation of any extended X-ray emission. For those objects with evidence for statistically significant extended X-ray lobes (4C 41.17 and 4C 03.24), we combine the *Chandra* measurements with literature data at lower frequencies to assemble the systems' spectral energy distributions (SEDs), and utilize state-of-the-art SED modelling – including emission from the disc, torus, jet, hotspots and lobes – to infer their physical parameters. For both radio galaxies, the magnetic energy density in the hotspots is found to exceed the energy density in CMB photons, whereas the opposite is true for the lobes. This implies that any extended synchrotron emission likely originates from the hotspots themselves, rather than the lobes. Conversely, inverse Compton scattering of CMB photons dominates the extended X-ray emission from the lobes, which are effectively 'radio-quenched'. As a result, CMB quenching is effective in these systems in spite of the fact that the observed X-ray to radio luminosity ratio does not bear the signature $(1 + z)^4$ dependence of the CMB energy density.

Key words: radiation mechanisms: non-thermal – galaxies: active – galaxies: high-redshift – galaxies: jets – X-rays: galaxies.

1 INTRODUCTION

Radio synchrotron emission from jetted active galactic nuclei (AGNs) arises from magnetized plasma within collimated, relativistic jets, plus the jet-inflated lobes, including the hotspots. If the observer line of sight lies within an angle $\sim 1/\Gamma$ of the jet axis, where Γ is the jet bulk Lorentz factor, then the beamed jet emission dominates the energy spectrum, and the system is classified as a blazar ($\Gamma \simeq 10$–15 for typical blazars). For large viewing angles, isotropic emission from the extended lobes takes over, and a powerful radio galaxy is observed. From simple beaming arguments, it follows that, for each observed blazar, there ought to be $\sim 2\Gamma^2$ misaligned, jetted AGNs. The identification of more than a dozen high-redshift blazars ($z \gtrsim 4$) (e.g. Yuan et al. 2006; Sbarrato et al. 2013, 2015; Wu et al. 2013, and the references therein) implies the existence of a much larger population of jetted AGNs only $\lesssim 1.5$ Gyr after the Big Bang. Nevertheless, in spite of being well within the detection threshold of modern wide-field radio surveys (such as the FIRST survey[1]), this high-z 'parent population' remains

[1] Faint Images of the Radio Sky at Twenty Centimeters (Becker, White & Helfand 1995).

★ Email: jfwu@umich.edu

© 2017 The Authors
Published by Oxford University Press on behalf of the Royal Astronomical Society

Downloaded from https://academic.oup.com/mnras/article-abstract/468/1/109/3038247 by inaf user on 13 July 2020

elusive. Volonteri et al. (2011) find that the expected number density of radio-loud quasars – as inferred from the hard X-ray detected, BAT[2] sample of luminous, massive blazars (Ajello et al. 2009) – significantly overestimates the number of observed luminous, *radio-loud quasars* detected by the SDSS[3] at $z \gtrsim 3$. Qualitatively similar conclusions are reached by Ghisellini & Sbarrato (2016) and Kratzer & Richards (2015) (see also Haiman, Quataert & Bower 2004; McGreer, Helfand & White 2009).

Possible explanations for this apparent deficit include (e.g. Volonteri et al. 2011) selection biases, such as heavy optical obscuration by dust; systematic, intrinsic differences in the jets' physical properties at high-z compared to the local population (such as lower average Γ factor) and/or intrinsic dimming of the radio lobes. The first hypothesis implies the existence of a large population of infrared-luminous, radio-loud quasars with no detectable optical counterparts, whereas the second appears at odds with the notion of the most powerful jets being associated with high accretion rates, likely typical at early cosmic times.

With respect to the third hypothesis, an attractive possibility is that of cosmic microwave background (CMB) photons affecting the behaviour of jetted AGNs (e.g. Celotti & Fabian 2004; Mocz, Fabian & Blundell 2011). In a series of recent works, Ghisellini et al. (Ghisellini et al. 2014, 2015; Ghisellini & Sbarrato 2016) explore specifically how the interaction between the CMB radiation and electrons within jet-powered lobes affects the observational appearance of jetted AGNs at different redshifts. Simply put, owing to its $(1 + z)^4$ dependence, the CMB energy density likely starts to dominate magnetic energy density within the lobes above $z \simeq 3$. As a result, synchrotron radio emission is progressively suppressed at higher redshifts, while the high-energy electrons cool effectively by inverse Compton scattering off of CMB photons (IC/CMB). The cooling time-scale of the IC/CMB mechanism at high redshifts is much shorter than typical jet lifetime (see the formulation in section 2.2 of Ghisellini et al. 2014). For example, at $z \gtrsim 3$, for electron Lorentz factor of $\gamma \sim 4 \times 10^3$, the cooling time $\gamma/\dot{\gamma} \sim 2$ Myr. This leads to dimming in the radio and enhancement in the X-rays. Even if the CMB energy does not exceed the typical jet or hotspot magnetic energy density, one nonetheless expects radio dimming and X-ray enhancement in these features as well, and IC emission is seen in high-z X-ray jets (e.g. Siemiginowska et al. 2003; Cheung, Stawarz & Siemiginowska 2006; Cheung et al. 2012; McKeough et al. 2016). Systems where IC/CMB cooling is dominant would then be classified as radio-quiet despite being jetted AGNs.

Even though most high-z radio-loud quasars in the FIRST survey are 'core dominated' in maps with a 5 arcsec beam size, this does not mean that all quasars with powerful jets are dominated by a flat-spectrum core where the IC/CMB mechanism would not work. Indeed, many of the core-dominated systems are steep-spectrum radio quasars (SSRQs) that are associated with misaligned jets and are evidently not dominated by the flat-spectrum core associated with blazars and the pc- or kpc-scale jets in local radio galaxies. Many of the core-dominated systems may be small radio galaxies analogous to low-z compact-steep-spectrum sources, since at $1 < z < 4$ the FIRST beam corresponds to 35–40 kpc. From a physical standpoint, powerful jetted AGN share the basic features of a jet, a terminal shock at the interface of the jet head and surroundings and spent jet material downstream that is associated with the radio lobes. Thus, the enhanced IC scattering could be relevant for any SSRQ, and we expect that the SSRQs comprise most of the 'missing' sources, since flat-spectrum radio quasars (FSRQs) are identified with blazars.

This paper is concerned with the IC/CMB hypothesis for 'missing' radio-loud quasars. Although the CMB energy density dependence with redshift is well established, directly testing this hypothesis requires measuring magnetic energy densities, which is challenging even for nearby systems. An alternate approach is to search for radio-quiet quasars with X-ray jets or lobes. A census of hard X-ray jets and lobes in radio-quiet quasars would show how much of the discrepancy between blazars and radio-loud quasars the IC/CMB hypothesis can explain. However, this is observationally challenging because typical SSRQ radio-lobe luminosities, cast to the hard X-rays at $z > 3$, require deep (100 ks) *Chandra* exposures to be detected, and they could also be confused with diffuse X-ray emission or be impossible to see against the backdrop of the intrinsic AGN X-ray emission. In addition, there is no *a priori* knowledge of which radio-quiet quasars to target. *XMM–Newton* has an angular resolution that is 12 times worse than *Chandra*, and would only be sensitive to large lobes in addition to the other problems. Moreover, as exemplified by the results from deep *XMM–Newton* imaging observations of two of the highest redshift radio-quiet quasars (ULAS J1120+0641, at $z = 7.1$, and SDSS J1030+0524, at $z = 6.3$), even in the absence of extended X-ray emission, the resulting upper limits could still be reconciled with the presence of extremely powerful – and yet undetected – jets (Mocz, Fabian & Blundell 2013; Fabian et al. 2014).

Another approach is to estimate the typical dimming based on X-ray emission from known radio systems, and then extrapolate to estimate how many systems would be undetected in the radio. To first approximation, if CMB-quenching of high-z radio lobes is effective, one would expect the ratio between X-ray luminosity and radio luminosity $L_X/L_{\rm radio}$ to increase with z, eventually leading to the disappearance of most radio lobes. Ghisellini et al. (2015) show that *none* of the 13 known $z > 4$ blazars show evidence for extended radio emission in their GHz spectra, which is inferred from the lack of spectral softening below the 1 GHz rest-frame emission and supports CMB quenching. Meanwhile, Wu et al. (2013) find that $z \gtrsim 4$ blazars exhibit a modest X-ray enhancement by a factor of ~3 compared to lower redshift counterparts with similar radio luminosity, optical/UV luminosity and radio loudness. Simply based on luminosity ratios, this supports the scenario of CMB photon upscattering, but only on a fractional basis, i.e. ~6 per cent of the X-ray emission at $z \sim 1$ is from IC/CMB, and this fraction increases to ~70 per cent at $z \sim 4$. This supports the increasing importance of IC/CMB cooling at high-z but not to the same extent. On the other hand, Smail et al. (2012) find no evidence for a $(1 + z)^4$ increase in $L_X/L_{\rm radio}$ for a sample of 10 powerful radio galaxies between $1.8 < z < 3.8$. One possible explanation for the lower-than-expected $L_X/L_{\rm radio}$ ratio is that most of the seed photons for IC scattering in these systems are locally produced, far-IR photons from star formation as opposed to CMB photons (Smail & Blundell 2013). Another possible explanation is that the radio and X-ray emission mostly come from separate regions in the system due to spatial variation in the ratio of photon and magnetic energy densities, in which case the total $L_X/L_{\rm radio}$ is not meaningful. For example, the jet or hot spots may have a particularly high magnetic energy density, whereas the dimming could work as expected in the lobes.

One way to avoid this issue is to decompose the radio and X-ray emission through high fidelity, high-resolution images. However, in general, the available multiwavelength data have a range of beam sizes, many of which are large. This leads to some ambiguity when

[2] Burst Alert Telescope, onboard the *Swift* satellite (Krimm et al. 2013).
[3] Sloan Digital Sky Survey (York et al. 2000).

Downloaded from https://academic.oup.com/mnras/article-abstract/468/1/109/3038247 by inaf user on 13 July 2020

Table 1. High-z radio galaxies and their *Chandra* observations. References: (1) Smail et al. (2012); (2) Scharf et al. (2003); (3) Smail et al. (2009); (4) Smail & Blundell (2013). The coordinates are of the point X-ray source. The exposure time has been corrected for background flares and detector dead time.

Name	R.A. (J2000)	Dec. (J2000)	z	Obs. ID	Date	Exposure time (ks)	References
4C 03.24	12:45:38.38	+03:23:21.5	3.57	12288	2010-12-05	90.6	1
4C 19.71	21:44:07.51	+19:29:15.1	3.59	12287	2010-08-23	36.0	1
				13024	2010-08-26	53.7	
4C 41.17	06:50:52.18	+41:30:31.2	3.79	3208	2002-09-25	63.2	2
				4379	2002-09-26	73.7	
4C 60.07	05:12:55.10	+60:30:51.1	3.79	10489	2008-12-10	98.7	3
TN J1338−1942	13:38:26.11	−19:42:31.3	4.11	5735	2005-08-29	30.4	4
				6367	2005-08-31	21.3	
				6368	2005-09-03	21.5	

identifying radio and X-ray features. In addition, emission from jet knots is complex and can come from a range of physical conditions even in high-resolution images, and it is unclear how to extrapolate undetected jets (especially without knowing the viewing angle). Another issue is that the X-ray photons in the *Chandra* band typically come from lower energy electrons below the synchrotron peak, even at $z > 3$, whereas the radio fluxes are typically above the synchrotron peak. Connecting the two requires some model if the peak is not in the covered region. These issues motivate the approach adopted in this paper, which is to construct self-consistent models of jetted AGN based on Ghisellini et al. (2015) using a broad spectral energy distribution (SED) to determine the level of X-ray enhancement in the lobes. This allows for a comparison of the diffuse X-ray and radio emission in known radio galaxies. Our goal is to determine whether the lobe emission is consistent with the IC/CMB behaviour (as opposed to the case where the seed photons are from local star formation), in which case CMB quenching could turn sources where the luminosity is dominated by the diffuse component into radio-quiet quasars.

We focus here on the handful of high-z ($z \gtrsim 3.5$) radio-loud AGNs with deep *Chandra* imaging observations. We establish robust, conservative criteria to isolate a subset of objects with statistically significant, extended X-ray emission (Section 2). For those, we decompose the X-ray emission into core and extended (lobes + hotspots) components, and model the resulting broad-band SEDs following Ghisellini et al. (2015), accounting for both CMB as well as IR emission from the host galaxy as possible Comptonization seed photons (Section 3). We summarize and discuss our results in Section 4.

2 X-RAY DATA REDUCTION AND ANALYSIS

To allow a meaningful investigation of their extended emission, we focus on high-z radio galaxies – here defined as having $z > 3.5$ – with archival *Chandra* observations with total exposures exceeding 50 ks. This exposure time limit, though admittedly arbitrary, is necessary since the surface brightness of lobe X-ray emission is usually low (Croston et al. 2005). The sample is composed of five objects, whose observation logs are listed in Table 1.

All the five radio galaxies were observed with the Advanced CCD Imaging Spectrometer (ACIS; Garmire et al. 2003). Standard CIAO v4.7 scripts/procedures were employed to reduce the data. For each individual observation, we reprocessed the archival data and generated new level 2 event and bad pixel files using the script `chandra_repro` with the latest Calibration data base applied (CALDB v4.6.8). The algorithm EDSER (Energy-Dependent Subpixel Event Repositioning; Li et al. 2004) was applied as default, for the purpose of generating subpixel X-ray images (see below). The absolute astrometry was then corrected by matching an initial point source list, generated with the `wavdetect` algorithm (Freeman et al. 2002), to the source catalog of the Two Micron All Sky Survey (2MASS; Skrutskie et al. 2006) or the Sloan Digital Sky Survey Data Release 9 (SDSS DR9; Ahn et al. 2012). The typical positional error after the astrometric correction is between 0.2 arcsec (for 4C 41.17 that has higher *Chandra* counts) and 0.5 arcsec (for the other four objects).

If present, background flares (3σ above the average) were removed using the CIAO script `deflare` [filtered time intervals were minimal (<15 per cent) for all observations].

X-ray images were generated in the observer-frame soft (0.5–2.0 keV), hard (2.0–8.0 keV) and full (0.5–8.0) bands using events with ASCA grades 0,2,3,4,6. Exposure maps and PSFs were also produced for the full-band images. Source detection was then carried out again on the full-band images using `wavdetect`, with a detection threshold of 10^{-6} and wavelet scales of 1, $\sqrt{2}$, 2, $\sqrt{4}$ and 4 pixels. For objects with multiple epochs (4C 19.71, 4C 41.17 and TN J1338−1942), we merged the observations by reprojecting the level 2 event files with shorter exposure times to the one with the longest exposure time. With the merged event file, we repeated the above procedure for generating X-ray images, exposure maps, PSF and point source lists. Figs 1–3 show the full-band *Chandra* images for all the five radio galaxies.

Next, we aim to establish a quantitative criterion to determine whether the detected X-ray emission is point-like versus extended, and whether, in the presence of extended emission, its location and spatial extent are consistent with the position of the galaxies' radio lobes. The latter is typically done by comparing the source's measured photon density profile to that of the PSF. The results of this procedure are presented in the following subsections.

2.1 4C 41.17

4C 41.17 has been observed twice by *Chandra*, yielding a total (good) exposure time of 137 ks. The upper left panel of Fig. 1 shows the merged, full-band *Chandra* image, where the green open circle labels the position of the point X-ray source as identified by `wavdetect`. To inspect the source spatial profile, we first created a sub-pixel full-band X-ray image for 4C 41.17, shown in the upper right panel of Fig. 1. The pixel size in this image (≈0.12 arcsec) is chosen to be 1/4 of the native size of ACIS pixels. The image is smoothed with a 0.37 arcsec × 0.37 arcsec top-hat kernel using the `aconvolve` procedure. There appears to be an appreciable

Downloaded from https://academic.oup.com/mnras/article-abstract/468/1/109/3038247 by inaf user on 13 July 2020

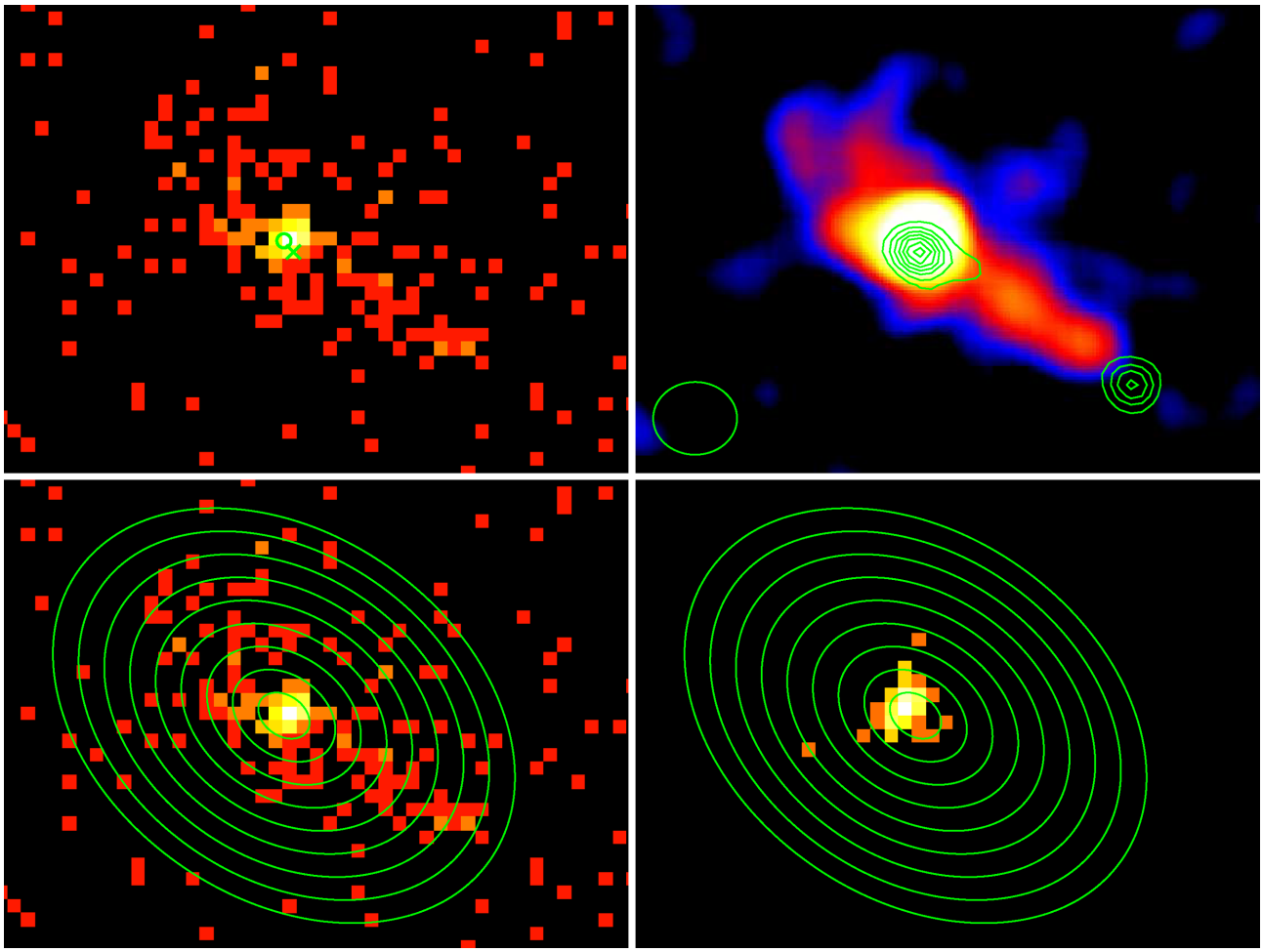

Figure 1. The *Chandra* ACIS images of 4C 41.17. The left two panels are the original full-band (0.5–8.0 keV) images. The upper right panel is the smoothed subpixel images, with the overlaid 1.4 GHz radio flux contours. The first level of the contours has the flux of 15 mJy beam^{-1}, while each subsequent level has a flux increase of 15 mJy beam^{-1}. The beam size is shown as the ellipse in the bottom left corner of this panel, with semimajor axis of 1.5 arcsec and semiminor axis of 1.3 arcsec. The lower right panel is the ChaRT simulated PSF for the *Chandra* observations. In the upper left panel, the open circle and the cross symbol label the X-ray position and the radio position of the point source, respectively. The elliptical annular regions in the lower panels are those used in calculating the profile of the X-ray count number density for the extended X-ray emission.

elongated structure in the SW–NE direction, superimposed to the nuclear emission. We will proceed with a quantitative analysis of this structure below.

Overlaid on the X-ray image are the contours of the 1.4 GHz radio emission, generated from the NRAO VLA Archive Survey Images.[4] The *A* and *B* radio components defined in Chambers, Miley & van Breugel (1990) and Carilli, Owen & Harris (1994) are shown. The *A* component can be seen as a compact radio knot at the position consistent with the edge of the elongated extended X-ray emission. High-frequency radio images in Carilli et al. (1994) reveal double hotspots within the *A* component. The *B* component is closely associated with the core X-ray emission. However, it is difficult to ascertain its physical nature based on the radio map. While Chambers et al. (1990) argue that no flat-spectrum radio core is detected, Carilli et al. (1994) claim the detection of radio core at 4.7 and 8.3 GHz, the position of which is labelled by the green cross in the upper-left panel of Fig. 1. The offset between the X-ray and radio coordinates is ≈0.6 arcsec, which is comparable to the typical 90 per cent uncertainty circle of the *Chandra* absolute position. We note, however, that the spectral index of the claimed radio core is quite inverted (≈−0.7 between 4.7 and 8.3 GHz), making the identification of a self-absorbed, compact radio nucleus somewhat debatable.

PSF profiles were simulated using the *Chandra* Ray Tracer (ChaRT; Carter et al. 2003). Spectra of the central point source (using a circular aperture of 2 arcsec radius) and the background (using an annular region with the inner and outer radii of 10 arcsec and 15 arcsec, respectively) were extracted using `specextract`, within SHERPA (Freeman, Doe & Siemiginowska 2001). The saved spectra, together with the corrected aspect solution file, were input to the ChaRT server.[5] The output ray tracing file was then fed into the MARX simulator[6] (Davis et al. 2012) to create the simulated PSF event file (shown in the lower right panel of Fig. 1). To calculate the radial profile of the background-subtracted source photon density, we adopted a series of concentric elliptical annular regions

[4] https://archive.nrao.edu/nvas/

[5] http://cxc.harvard.edu/ciao/PSFs/chart2/runchart.html

[6] http://space.mit.edu/cxc/marx/

Downloaded from https://academic.oup.com/mnras/article-abstract/468/1/109/3038247 by inaf user on 13 July 2020

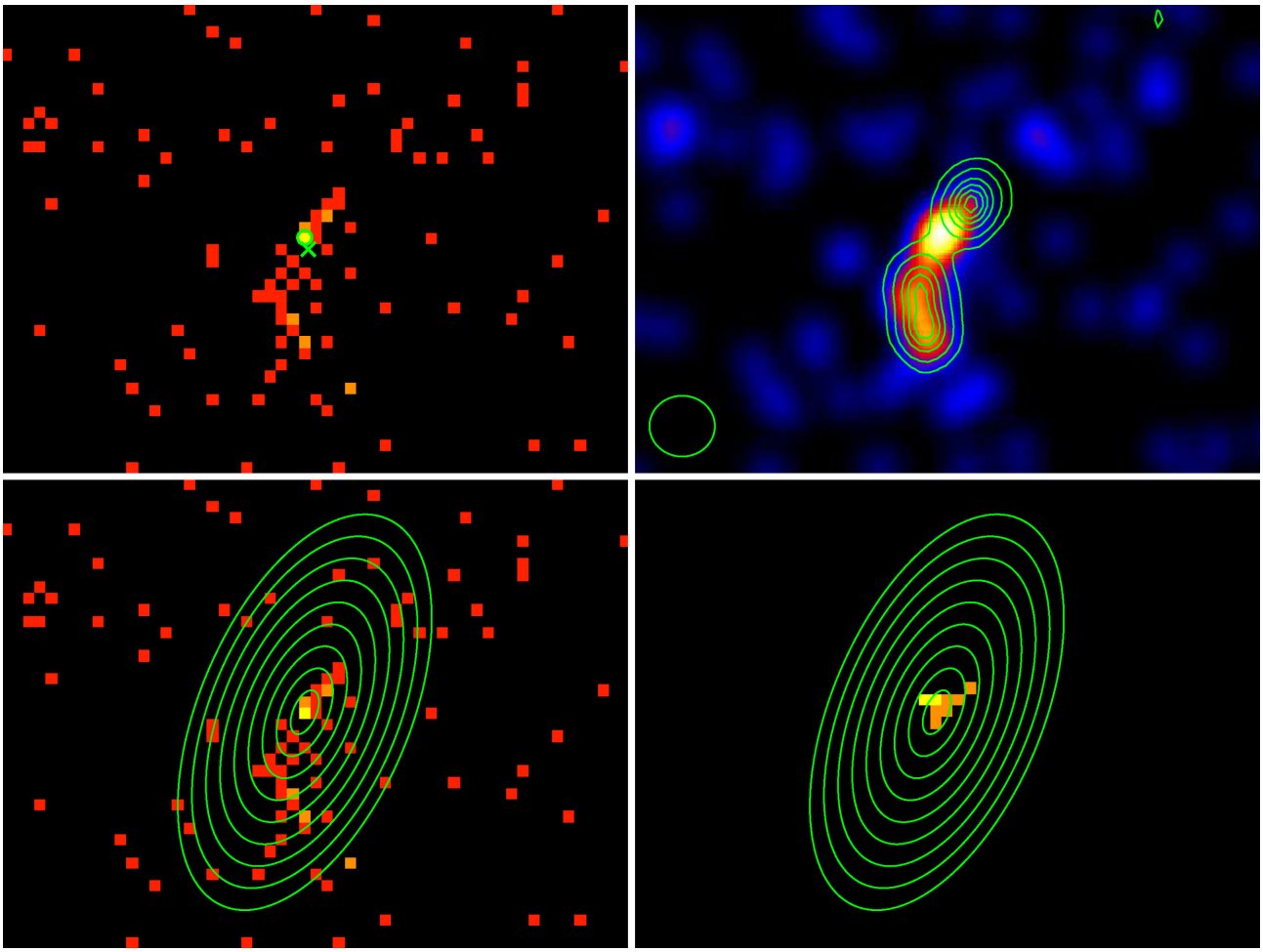

Figure 2. The *Chandra* ACIS images of 4C 03.24. The left two panels are the original full-band (0.5–8.0 keV) images. The upper right panel is the smoothed subpixel images, with the overlaid 1.4 GHz radio flux contours. The contour levels are 2, 10, 25, 40, 65 and 90 mJy beam^{-1}. The beam size is shown as the ellipse in the bottom left corner of this panel, with semimajor axis of 1.4 arcsec and semiminor axis of 1.3 arcsec. The lower right panel is the ChaRT simulated PSF for the *Chandra* observation. In the upper left panel, the open circle and the cross symbol label the X-ray position and the radio position of the point source, respectively. The elliptical annular regions are those used in calculating the profile of the X-ray count number density for the extended X-ray emission.

(see the contours in the lower panels of Fig. 1),[7] with semimajor axes between 1 arcsec and 9 arcsec with steps of 1 arcsec, and the semiminor axes between 0.72 arcsec and 6.5 arcsec, with steps of 0.72 arcsec. The size parameters are chosen to ensure that the extended X-ray emission can be covered by a series of ∼10 annuli. Minor changes to these parameters will not affect our results below on assessing the existence of extended emission. The positioning angle of the annuli is 325°, which is visually determined to be approximately along the direction of the extended emission.

A direct comparison of the radial profile of the source photon density profile for 4C 41.17 (solid line) against the simulated PSF's (dashed line), shown in Fig. 4, confirms the presence of a statistically significant extended component that goes well beyond 2 arcsec off the central point source in 4C 41.17.

The measured photon density outside the central 2 arcsec declines following roughly an exponential law, and becomes indistinguishable from the background level beyond 8 arcsec. To estimate the total X-ray counts within the extended emission, we fit an exponential law (corresponding to a linear relation if the photon density is in log-scale) between 2 arcsec and 8 arcsec and then extrapolated it into inside 2 arcsec, yielding a total of $111.9^{+11.6}_{-10.6}$ counts over the full energy band. This was then subtracted from the total X-ray counts measured within a 8 arcsec radius to obtained the total point source counts, which is $66.5^{+9.2}_{-8.1}$, where the quoted uncertainties are at the 1σ confidence level (Gehrels 1986).

Lastly, we analysed the basic spectral properties of the extended emission and the point source. We extracted the spectra from the (two) unmerged *Chandra* observations, and fit them jointly. Spectra for the extended emission were extracted from annular regions between 2 arcsec and 8 arcsec, while the spectra of the point source were extracted from circular regions within 2 arcsec. The background spectra were extracted from annular regions between 10 arcsec and 15 arcsec. The resulting spectra were binned to at least one count per bin (i.e. to eliminate zero count channels), and analysed with the XSPEC package v.12.9.0 (Arnaud 1996) using *C*-statistic (Cash 1979), which is best suited for low number count spectra (Nousek & Shue 1989). For modelling purposes, we adopted an absorbed power-law model (`wabs`; Morrison &

[7] We acknowledge that without prior knowledge of the spatial profile of the extended emission, circular annuli should be the default choice over elliptical ones. We also calculated the radial photon density with circular annular regions and obtained consistent results.

Downloaded from https://academic.oup.com/mnras/article-abstract/468/1/109/3038247 by inaf user on 13 July 2020

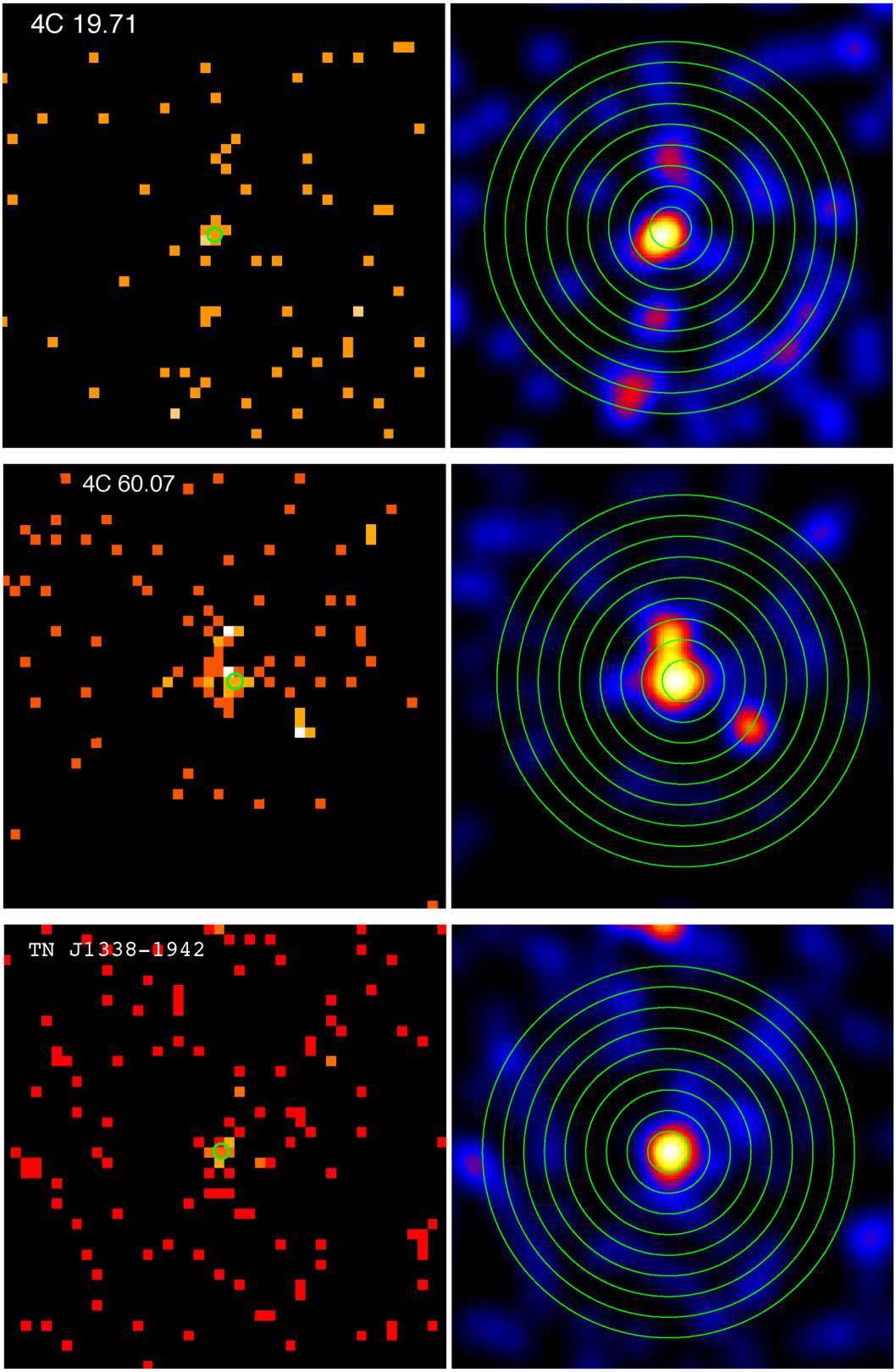

Figure 3. The *Chandra* ACIS images of 4C 19.71 (top), 4C 60.07 (middle) and TN J1338−1942 (bottom). For each object, the raw, full-band (0.5–8.0 keV) image is shown on the left, while the smoothed subpixel image is shown on the right. The open circles in the left-hand panels label the position of the X-ray point sources. The green annular regions in each right-hand panel are those used in calculating the profile of the X-ray count number density for the extended X-ray emission. None of thee objects shows evidence for a statistically significant extension in the X-ray emission.

Downloaded from https://academic.oup.com/mnras/article-abstract/468/1/109/3038247 by inaf user on 13 July 2020

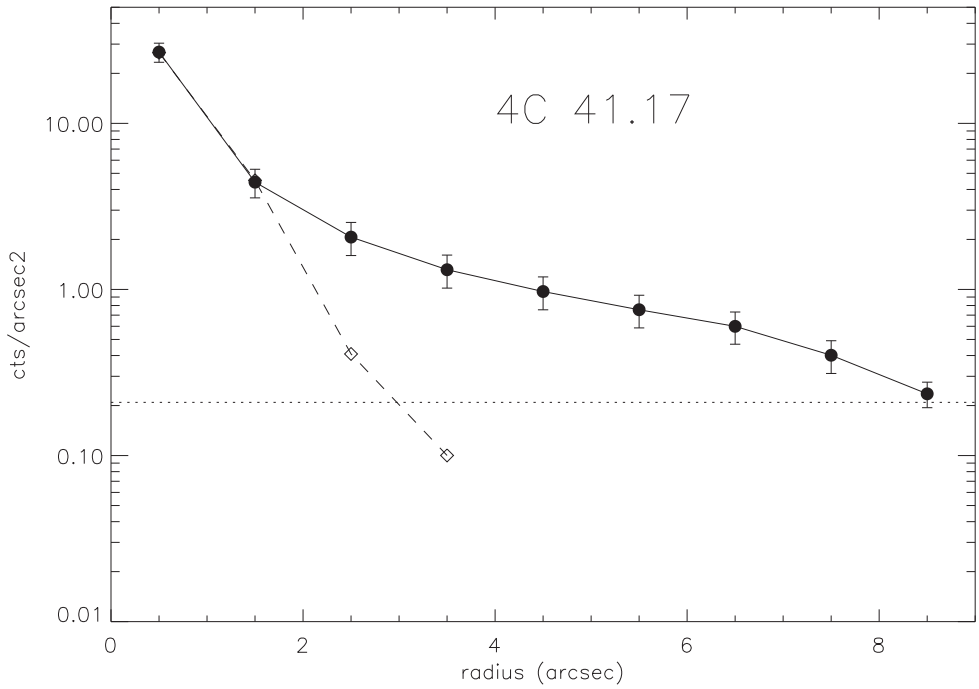

Figure 4. The photon density profile of 4C 41.17 (solid line) is shown versus the simulated PSFs (dashed line). The source's profile is calculated along the major axes of the elliptical regions shown in Fig. 1. The dotted horizontal line indicates the background value.

McCammon 1983), with hydrogen column density fixed at the Galactic value: $N_{\rm H} = 1.07 \times 10^{21}$ cm^{-2} that is calculated using the COLDEN tool.[8] The resulting photon index from the joint fitting is $\Gamma = 1.6 \pm 0.4$, yielding a full-band, observer-frame flux of $F_{\rm X} = 6.56^{+0.68}_{-0.62} \times 10^{-15}$ erg cm^{-2} s^{-1} for the extended emission. The fitting statistic $C/n = 89.4/93$, where C is the C-statistic and n is the number of bins. The spectra of the point source were fit using the same model. The resulting X-ray photon index, $\Gamma = 0.8 \pm 0.3$, is much harder than that of the extended emission, possibly indicating strong intrinsic absorption, or a different emission mechanism. The full-band flux is $F_{\rm X} = 6.48^{+0.89}_{-0.79} \times 10^{-15}$ erg cm^{-2} s^{-1}. For the point source, $C/n = 91.9/102$.

2.2 4C 03.24

A similar procedure to above-described procedure for 4C 41.17 was adopted to analyse the ACIS data of 4C 03.24, consisting of one observation with (good) exposure time of 90.6 ks. The full-band, raw X-ray image and the smoothed subpixel (0.12 arcsec) image are shown in the top panels of Fig. 2. A point X-ray source is clearly detected. Extended X-ray lobes appear to be along the NW-S direction.

The 1.4 GHz radio contours are also shown in the upper right panel, overlaid on the smoothed X-ray image. The extended radio emission along the S-direction is aligned with the extended X-ray emission, while the radio knot along the NW-direction near the edge of the X-ray lobe can possibly be considered as a radio hotspot. van Ojik et al. (1996) provided 1.5 GHz, 4.7 GHz and 8.3 GHz radio maps (see their figs 3 and 4). A radio core is detected at 4.7 GHz and 8.3 GHz, albeit with a steep spectral index, too (≈ -1.2). This radio core is $\approx$0.5 arcsec away from the point X-ray source.

To assess the statistical significance of the extended X-ray emission, we defined a series of concentric elliptical annuli with semi-major axes between 1 arcsec and 9 arcsec with steps of 1 arcsec, and semiminor axes between 0.5 arcsec and 4.5 arcsec with steps of 0.5 arcsec (see the lower panels of Fig. 2). The positioning angle is 67°. The PSF was again simulated with ChaRT and MARX, following the same procedure as outlined above (lower right panel of Fig. 2). The radial photon density profiles of 4C 03.24 is compared to the simulated PSFs in Fig. 5, showing evidence for extended X-ray emission beyond 1 arcsec. The total, full-band counts for the extended emission and the point-source are $34.1^{+6.9}_{-5.8}$ and $4.6^{+3.3}_{-2.1}$, respectively.

As for 4C 41.17, we extracted and analysed the extended emission and point source spectra; the hydrogen column density was fixed at the Galactic value: $N_{\rm H} = 1.92 \times 10^{20}$ cm^{-2}. For the extended emission, the best-fitting photon index is $\Gamma = 1.4 \pm 0.6$ ($C/n = 17.9/25$). The unabsorbed full-band flux is $F_{\rm X} = 4.69^{+0.93}_{-1.27} \times 10^{-15}$ erg cm^{-2} s^{-1}. For the point source, $\Gamma = 1.2^{+0.8}_{-0.4}$ ($C/n = 5.1/13$). The unabsorbed full-band flux is $F_{\rm X} = 2.41^{+1.02}_{-0.87} \times 10^{-15}$ erg cm^{-2} s^{-1}. For both 4C 41.17 and 4C 03.24, it is not feasible to decompose the diffuse emission component from the core source inside the 2 arcsec-radius circular region due to insufficient counts.

2.3 4C 19.71, 4C 60.07 and TN J1338−1942

The full-band and sub-pixel images of the remaining three high-redshift radio galaxies with deep *Chandra* data are presented in Fig. 3: as discussed next, contrary to what was reported in the literature listed in Table 1, *we could not confirm the presence of statistically significant extended X-ray emission associated with the radio lobes in these objects*.

[8] http://cxc.harvard.edu/toolkit/colden.jsp (Dickey & Lockman 1990). Including an extra component to account for intrinsic absorption and/or allowing the hydrogen column density to vary did not yield any improvement in the fitting.

Downloaded from https://academic.oup.com/mnras/article-abstract/468/1/109/3038247 by inaf user on 13 July 2020

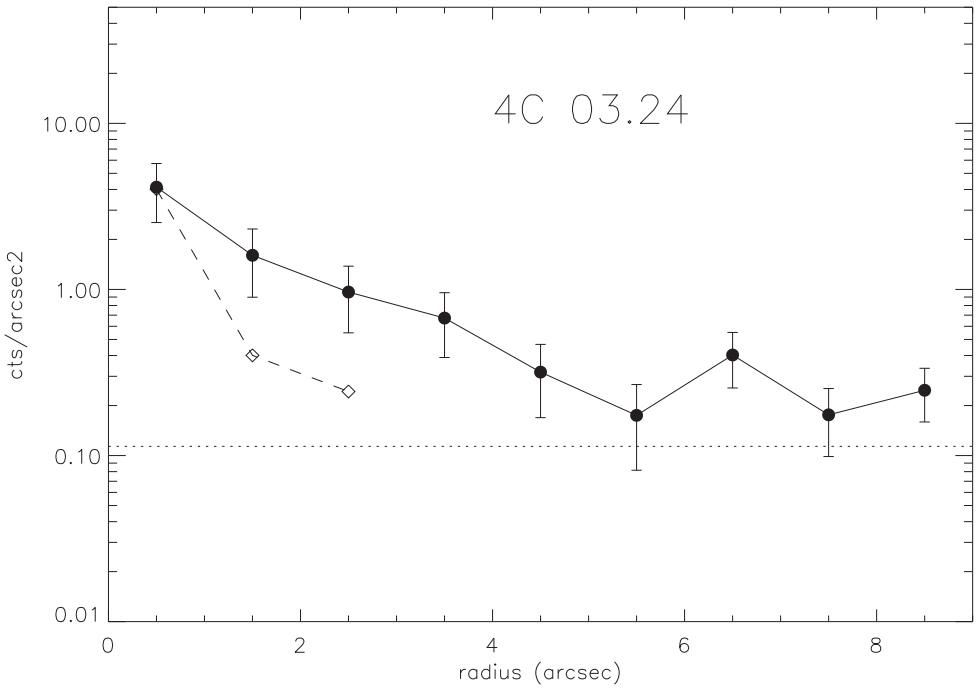

Figure 5. Photon density profile of 4C 03.24 (solid line) versus the simulated PSFs (dashed line). The source's profile is calculated along the major axes of the elliptical regions shown in Fig. 2. The dotted horizontal line indicates the background value.

A bright, point-like X-ray source was detected at a position consistent with the optical source position in each target. In line with the previous two cases, we derived the sources' radial photon density profiles and compared them to the simulated PSFs' profiles (see Fig. 6). For 4C 19.71, the detected X-ray source's radial profile decreases so rapidly that it is consistent with background beyond 2 arcsec, similar to the simulated PSFs (top panel of Fig. 6). The X-ray image might suggest the presence of possible, off nuclear X-ray sources located 4 arcsec and 5 arcsec away from the central point source in the N and S direction, respectively (see the top right panel of Fig. 3). The detection of co-spatial 8.3 GHz radio lobes at these positions (Smail et al. 2012) admittedly increases the probability that such extended X-ray emission is indeed present. However, from a statistical perspective, none of the visual enhancements represents a significant detection above the background.

For 4C 60.07, the radial photon density exceeds the background level within ∼5 arcsec from the central X-ray source position (middle panel of Fig. 6). This excess emission appears to be mainly composed by two off-nuclear sources, respectively ≈3 arcsec away in the N direction and ≈5 arcsec away in the SW direction (see the middle right panel of Fig. 3). However, these sources are located in a direction that is nearly *perpendicular* to that of the galaxy radio lobes (see fig. 1 of Smail et al. 2009). At the same time, the measured X-ray counts within the region corresponding to the location of the radio lobes are consistent with the background level.

The radial photon density profile of TN J1338−1942 is entirely consistent with the PSF's profile (bottom panel of Fig. 6). It reaches the background level beyond 2 arcsec.

In summary, we find no compelling, statistically significant evidence for extended X-ray emission that is co-spatial with the known radio lobes in any of the three sources considered here (albeit marginal evidence is found for 4C 19.71). For the SED modelling purposes, the X-ray upper limits cannot provide meaningful constraints on their SEDs. We will then focus on 4C 41.17 and 4C 03.24, for which we demonstrated the presence of significant, extended X-ray emission spatially associated with the known radio lobes. It is worth noting that the non-detection of extended X-ray emission does not necessarily rule out the existence of X-ray jets and/or lobes (e.g. see discussion in Fabian et al. 2014).

One caveat is that the above methodology of using annular regions to verify the existence of extended X-ray emission has its limits. It is most effective at searching for diffuse X-ray emission superimposed upon a centre point source. However, in case of two or more well-separated point sources, e.g. the core and the jet knots, it is difficult to reach definitive conclusion without visually inspecting the X-ray image. None of the five objects examined here suffer from this potential issue except 4C 60.07, for which, as discussed above, the two point X-ray sources in addition to the centre core are not likely associated with the radio galaxy.

3 OBSERVED SEDS

The SEDs of 4C 41.17 and 4C 03.24 are shown in Figs 7 and 8, respectively, where the total emission corresponds to the black open circles, whereas, whenever a decomposition was possible, the point source and extended emission are marked by blue and green circles, respectively. All the circle symbols represent observed data, while the modelling of the SEDs are detailed in the next section. The nature of the point radio sources is discussed in detail below. For the X-ray data points, the full band was broken into four sub-bands for 4C 41.17 (B1: 0.5–1.0 keV; B2: 1.0–2.0 keV; B3: 2.0–4.0 keV; B4: 4.0–8.0 keV), where the flux densities are expressed at the geometric mean frequency of each sub-band (see Table 2). Since both extended and point source component in 4C 03.24 have significantly fewer counts than those in 4C 41.17, for this system, we divided the full band into the two standard sub-bands: the soft band (0.5–2.0 keV) and hard band (2.0–8.0 keV; again see Table 2).

Downloaded from https://academic.oup.com/mnras/article-abstract/468/1/109/3038247 by inaf user on 13 July 2020

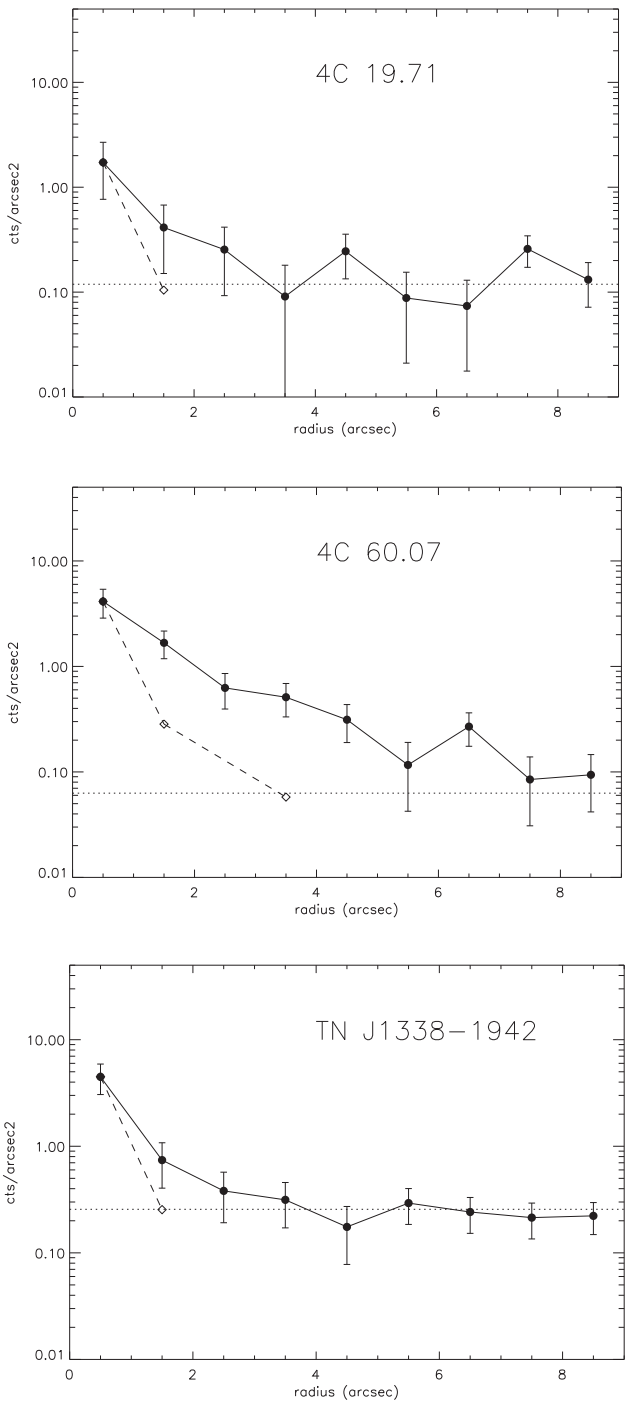

Figure 6. The radial photon density profiles for 4C 19.71, 4C 60.07 and TN J1338−1942 (solid lines), and the corresponding simulated PSF (dashed lines). The horizontal dotted line in each panel represents the photon density of the background. The profiles of the radio galaxies are calculated along the radii of the annular regions shown in the right panels of Fig. 3.

Flux densities in the radio, sub-millimeter, infrared and optical bands were retrieved from the NASA/IPAC Extragalactic Database (NED).[9] For most of these SED data points, only the total flux is available. Owing to the limited angular resolution of the

[9] http://ned.ipac.caltech.edu

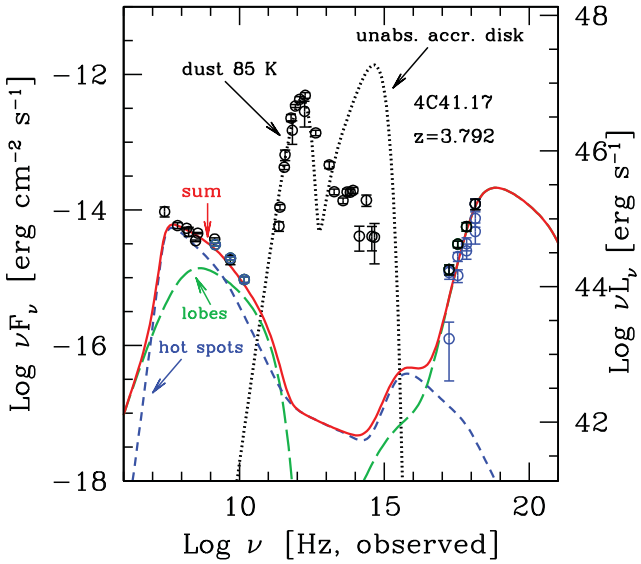

Figure 7. The SED of 4C 41.17 and the applied models. The open circles (and error bars) are the observed SED data points. The black dotted line corresponds to contribution of an accretion disc and absorbing dust, re-emitting in the IR as a blackbody of temperature $T_{\rm IR} = 85$ K. This material can correspond to an absorbing torus close to the accretion disc and/or some extra absorbing material in the host galaxy at large distances from the disc. We show the *unabsorbed* disc emission, that corresponds to a luminosity $L_{\rm d} = 2.6 \times 10^{47}$ erg s^{-1}. The inverse Compton flux from the jet is below the scale of the figure. The short-dashed blue line correspond to the emission from the hotspots (with parameters listed in Table 4). It contributes mainly to the low frequency radio emission. The long-dashed green line is the flux produced by the lobes (parameters in Table 4) contributing to the high frequency radio emission and especially to the X-ray flux. The solid red line is the sum of the hotspot and lobe fluxes.

corresponding observations, we typically only tabulate the total flux densities at each available frequency. However, high angular resolution radio maps are available for both 4C 41.17 and 4C 03.24, enabling us to attempt a core versus lobe decomposition at GHz frequencies. This is briefly discussed next.

As discussed in Section 2.1, 4C 41.17 has several components of extended radio emission, while the existence of a compact radio core is debatable. Regardless, the flux density of the alleged radio core is substantially lower (by a factor of >40) than that of the extended radio emission, thus having negligible effects on the estimated total flux density. Therefore, for SED modelling purposes, we choose to adopt the radio flux densities at 1.5 GHz, 4.9 GHz and 14.7 GHz given by Chambers et al. (1990).

For 4C 03.24, radio flux densities at 4.7 GHz, and 8.3 GHz are retrieved from table 2 of van Ojik et al. (1996), in which the *N* component is considered as the 'radio core', while other components combined as the extended radio emission.

4 SED MODELLING

Following Ghisellini et al. (2015), and references therein, we model the broad-band SEDs of 4C 41.17 and 4C 03.24 as arising from the superimposition of several components: (i) an accretion disc plus absorbing torus (and/or absorbing dust within the host galaxy); (ii) a (misaligned), compact, relativistic jet; (iii) two, relatively compact hotspots (which are assumed at rest), corresponding to the jet termination shocks and (iv) two extended lobes. The purpose of the SED modelling is to determine the radiation mechanism

Downloaded from https://academic.oup.com/mnras/article-abstract/468/1/109/3038247 by inaf user on 13 July 2020

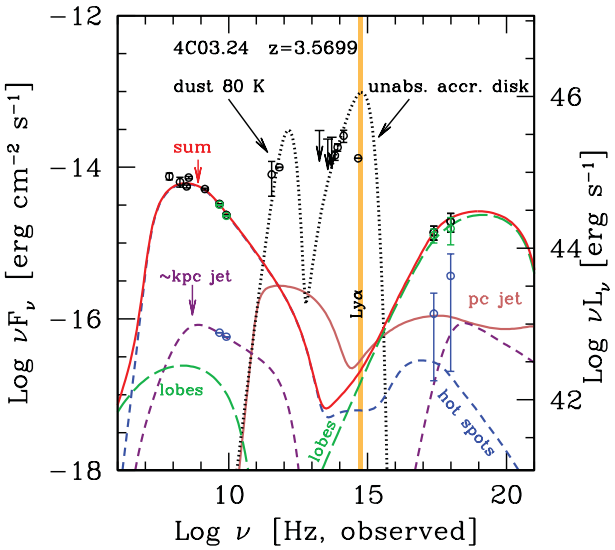

Figure 8. The SED of 4C 03.24 and the applied model. The open circles (and error bars) are the observed SED data points. The black dotted line corresponds to contribution of an accretion disc and absorbing dust, re-emitting in the IR as a blackbody of temperature $T_{\rm IR} = 80$ K. We show the *unabsorbed* disc emission, that corresponds to a luminosity $L_{\rm d} = 1.5 \times 10^{47}$ erg s^{-1}. The vertical orange line labels the observed-frame frequency of Lyα emission. The solid brown line is the emission produced by the inner (pc) relativistic jet, with parameters listed in Table 3. The synchrotron component of this emission is hidden below the dust and the disc emission, while the inverse Compton flux could contribute to the X–ray flux of the core. The violet dashed line corresponds to the emission from the jet, but at much larger (~kpc) scale. It is responsible for the relatively steep radio emission observed at the ~arcsec scale. The short-dashed blue line corresponds to the emission from the hotspots (with parameters listed in Table 4). It contributes mainly to the radio emission. The long-dashed green line is the flux produced by the lobes (parameters in Table 4) contributing to the X-ray flux. The solid red line is the sum of the hotspot and lobe fluxes.

Table 2. X-ray photometry for the high-z radio galaxies. The numbers for 'full-band' are the X-ray flux, in unit of 10^{-15} erg cm^{-2} s^{-1}. The numbers for the sub-bands are the X-ray flux density at a given frequency, in unit of 10^{-33} erg cm^{-2} s^{-1} Hz^{-1}.

Name	Band	Energy (keV)/ frequency (Hz)	X-ray flux/flux density Extended	Point source
4C 41.17	Full-band	0.5–8.0	$6.56^{+0.68}_{-0.62}$	$6.48^{+0.89}_{-0.79}$
	B1	1.71×10^{17}	7.0 ± 1.5	0.7 ± 0.6
	B2	3.42×10^{17}	6.0 ± 0.9	3.2 ± 0.7
	B3	6.84×10^{17}	3.7 ± 0.9	4.7 ± 1.0
	B4	1.37×10^{18}	5.5 ± 1.4	3.5 ± 1.2
4C 03.24	Full-band	0.5–8.0	$4.74^{+0.96}_{-0.81}$	$0.70^{+0.50}_{-0.32}$
	Soft-band	2.42×10^{17}	5.3 ± 1.1	0.5 ± 0.4
	Hard-band	9.67×10^{17}	1.6 ± 0.6	0.4 ± 0.4

for the observed flux in different bands, as well as the origin of the emission in case that decomposing into point and extended components is possible.

4.1 Disc/torus emission and black hole mass estimates

We assume a standard, geometrically thin, optically thick accretion disc (Shakura & Sunyaev 1973). The disc is surrounded by an absorbing torus, which intercepts the disc thermal emission and re-emits in the IR band.

For 4C 41.17, the broad-band SED shape indicates some level of absorption occurring in the optical band. We start by adopting a viewing angle ($\theta_{\rm v}$) that is offset by 45° with respect to the jet axis – which, in turn, coincides with the orthogonal to the inner disc. If the opening angle of the torus with respect to the jet axis is smaller than the viewing angle ($\theta_{\rm torus} < \theta_{\rm v}$), then the accretion disc emission as seen by the observer is absorbed.[10] Regardless, for the inferred disc luminosity, $L_{\rm d}$, not to exceed the Eddington limit, $L_{\rm Edd}$, the black hole mass, M, must exceed 2×10^9 M$_\odot$. In the following, we will adopt $M \sim 5 \times 10^9$ M$_\odot$, corresponding to $L_{\rm d}/L_{\rm Edd} \simeq 0.4$. Although the exact value of M is uncertain, this is not critical for the purpose of the SED modelling.

For 4C 03.24, the ratio between the observed IR and optical/UV emission is more typical of unabsorbed quasars; hence, $\theta_{\rm torus}$ likely exceeds $\theta_{\rm v}$ and the disc emission is not absorbed. Nevertheless, the highest frequency optical flux (i.e. rest frame UV, indicated the vertical line labelled 'Lyα' in Fig. 8) is likely absorbed by intervening Lyα clouds. The Lyα flux for this system corresponds to a Lyα luminosity of $\sim 2 \times 10^{44}$ erg s^{-1} (Roettgering et al. 1997); following Francis et al. (1991) and Vanden Berk et al. (2001), this corresponds to a broad-line luminosity $L_{\rm BLR} \sim 10^{45}$ erg s^{-1}. Further assuming that the broad lines re-emit 10 per cent of the disc flux, this yields $L_{\rm d} \sim 10^{46}$ erg s^{-1}. Adopting this value, the best agreement with the optical data is found for a black hole mass $M = 6 \times 10^8$ M$_\odot$ (corresponding to $L_{\rm d}/L_{\rm Edd} = 0.15$; lower disc luminosities would imply a larger black hole mass).

4.2 Jet emission

We assume that the total jet power – kinetic plus magnetic – is dissipated mostly in one zone (which, in turn, is responsible for producing the bulk of the radiation that is observed for very low viewing angle systems, such as blazars). This is not necessarily the case in radio galaxies, which are viewed at relatively large angles. For those, emission arising from the inner jet can still be detected if the viewing angle, $\theta_{\rm v}$, is not very large and/or the jet is 'structured', i.e. there is a gradient in bulk velocity and Lorentz factor, either as a function of the radial distance (accelerating or decelerating jets, e.g. Georganopoulos & Kazanas 2003), or the angular distance from the jet axis (i.e. a fast spine surrounded by a slower layer, Ghisellini, Tavecchio & Chiaberge 2005). For simplicity, we assume here that the jet is not structured, and is observed at an intermediate $\theta_{\rm v}$. We set $\theta_{\rm v} = 45°$ for 4C 41.17, and $\theta_{\rm v} = 17°$ for 4C 03.17, to account for the bright core X-ray emission (although if this X-ray component were instead produced by a somewhat less beamed portion of the jet, this would allow for somewhat larger values of $\theta_{\rm v}$).

The emission region is assumed to be spherical with a radius of $R = \psi R_{\rm diss}$, defined as the distance from the black hole, and ψ is the semi-aperture angle of the conical jet (we assume $\psi = 0.1$ rad). The region moves with velocity βc, corresponding to a bulk Lorentz factor Γ. Throughout, relativistic electrons are injected at a rate $Q(\gamma)$, embedded in a tangled magnetic field B and have total

[10] In this case, the 'core' radio emission reported by Carilli et al. (1994) cannot possibly be produced by the relativistic jet. However, the disc emission could also be absorbed by dust belts located at a relatively large distance from the black hole (and yet still within the host galaxy). In this case, $\theta_{\rm v}$ could be smaller, and the jet emission could indeed contribute to the 'radio core' identified by Carilli et al. (1994).

Downloaded from https://academic.oup.com/mnras/article-abstract/468/1/109/3038247 by inaf user on 13 July 2020

Table 3. Adopted parameters for the jet models shown in Figs 7 and 8. Col. [1]: name; Col. [2]: redshift; Col. [3]: black hole mass in solar masses; Col. [4]: disc luminosity in units of 10^{45} erg s^{-1}; Col. [5]: distance of the dissipation region from the black hole, in units of 10^{15} cm; Col. [6]: size of the BLR, in units of 10^{15} cm; Col. [7]: power injected in the jet in relativistic electrons, calculated in the comoving frame, in units of 10^{45} erg s^{-1}; Col. [8]: magnetic field in G; Col. [9]: bulk Lorentz factor; Col. [10]: viewing angle in degrees; Col. [11] and Col. [12]: break and maximum Lorenz factor of the injected electron distribution; Col. [13] and Col. [14]: slopes of the injected electron distribution; Col. [15]: logarithm of the total kinetic plus magnetic jet power, in erg s^{-1}. The values of the powers and the energetics refer to *one* jet.

Name [1]	z [2]	M [3]	L_d [4]	R_{diss} [5]	R_{BLR} [6]	$P'_{e,jet,45}$ [7]	B [8]	Γ [9]	θ_V [10]	γ_b [11]	γ_{max} [12]	s_1 [13]	s_2 [14]	$\log P_{jet}$ [15]
4C 41.17	3.792	5e9	260	2e3	1.6e3	0.01	1.6	12	45	100	4e3	1	3.4	47.2
4C 03.24 'pc'	3.57	6e8	11.7	108	342	0.06	5.3	10	17	100	3e3	0	2.0	46.9
4C 03.24 'kpc'	3.57	6e8	11.7	1.8e6	342	0.1	2e–4	3	17	600	4e4	–1	3.45	45.7

Table 4. Adopted parameters for the hotspot and lobe models shown in Figs 7 and 8. Col. [1]: name; Col. [2]: component (HS = hotspot); Col. [3]: size in kpc; Col. [4]: logarithm of the power injected in relativistic electrons in erg s^{-1}; Col. [5]: magnetic field in G; Col. [6] and Col. [7]: break and maximum Lorenz factor of the injected electron distribution; Col. [8] and Col. [9]: slopes of the injected electron distribution; Col. [10]: logarithm of the total energy in relativistic electrons, in erg; Col. [11]: logarithm of the total energy in magnetic field, in erg. The values of the powers and the energetics refer to *one* jet and *one* hotspot and lobe, while the lobe flux shown in the figures corresponds to *two* hotspots and lobes.

Name [1]	Comp. [2]	R [3]	$\log P_e$ [4]	B [5]	γ_b [6]	γ_{max} [7]	s_1 [8]	s_2 [9]	$\log E_e$ [10]	$\log E_B$ [11]
4C 41.17	HS	3.9	46.7	9.0e–4	100	1e5	–1	3.8	58.0	59.4
	lobe	48.7	46.1	1.7e–5	4e3	1e5	–1	2.8	59.3	59.2
4C 03.24	HS	4.9	45.9	9.0e–4	200	1e5	–1	3.0	57.5	59.7
	lobe	68.2	45.5	6.0e–6	900	7e4	1.3	2.3	59.0	58.7

power P'_e (measured in the comoving frame). The electron energy distribution, $Q(\gamma)$, is modelled as a double power law, with slopes s_1 and s_2 below and above the break energy, γ_b, respectively:

$$Q(\gamma) = Q_0 \frac{(\gamma/\gamma_b)^{-s_1}}{1+(\gamma/\gamma_b)^{-s_1+s_2}} \quad [\mathrm{cm^{-3}\ s^{-1}}]. \tag{1}$$

$Q(\gamma)$ extends between γ_{min} (assumed to be $\sim$1) and γ_{max}. Since we always assume that $s_1 \leq 1, s_2 > 2$, the exact value of γ_{max} is not critical. The particle density distribution, $N(\gamma)$ [cm^{-3}], is determined by solving the continuity equation at a time corresponding to the emission region light-crossing time, taking into account radiative cooling as well as pair production (albeit the latter is not relevant in our cases). Electrons radiatively cool by synchrotron and inverse Compton processes, with seed photons provided by the accretion disc, broad-line region (BLR), IR torus and CMB. The jet carries power in the form of Poynting flux P_B, along with bulk motion of electrons, P_e and protons, P_p. In addition, we account for the power P_r spent by the jet to produce the observed radiation. The corresponding parameters for the jet models are listed in Table 3.

We notice that, unlike for blazars, the contribution from the compact jet to the observed SED is going to be entirely negligible for 4C 41.17 and 4C 03.24. Nevertheless, the compact jet remains a key ingredient in the model, in that its kinetic jet power is directly related to the power injected in the lobes and hotspots in the form of magnetic field and relativistic electrons. Even though virtually none of the jet parameters can be directly constrained by modelling the systems' SEDs, its power is indirectly constrained by the observed optical emission via the known relation between jet power and accretion disc luminosity (Ghisellini et al. 2014). Thus, although the jet parameters listed in Table 3 cannot be thought of as 'best-fitting' parameters, they nevertheless provide us with a consistency check for the model, in that they need to not only be consistent with the measured upper limits (both to the radio and the optical emission, via the jet power relation to the disc luminosity), but also power the lobes and hotspots in such a way that the measured synchrotron and Compton luminosities satisfy the observational constraints.

For 4C 03.24, the observed radio emission at the arcsec scale has a relatively steep spectrum and cannot be accounted for the compact jet, whose radio spectrum is flat, or by the hotspots, that are of larger size. We are then obliged to consider another emission component, that we associate to the large scale jet, labelled in Fig. 8 and in Table 3 as 'kpc jet'.

4.3 Hotspot emission

The jet deposits its power into the hotspots through a termination shock, that in turn energizes the more extended lobes. To model the radiation produced in the hotspots, we follow the prescriptions detailed in Ghisellini et al. (2015). The particle injection function obeys equation (1), with different parameters from the jets. The hotspot sizes are assumed to be between 3 and 5 kpc, similarly to what is observed in nearby objects (such as Cygnus A, see Wilson, Young & Shopbell 2000). The amount of injected power, combined with the size, constrain the magnetic field and particle energy density (once the particle distribution is self-consistently derived by solving the continuity equation). Under these assumptions, we find that the hotspots in 4C 41.17 and 4C 03.24 have magnetic fields larger than the equipartition value with the electron energy. The magnetic energy density, U_B, is also found to exceed the CMB photon energy density, U_{CMB}. For non-moving sources, the magnetic field corresponding to equipartition with the CMB photon energy density is given by the expression:

$$B_{CMB} = 5.56 \times 10^{-5} \left(\frac{1+z}{4.5}\right)^2 \mathrm{G} \tag{2}$$

For both 4C 41.17 and 4C 03.24, the radio flux in both sources is dominated by the hotspots. As a consequence, the *radiative cooling is dominated by synchrotron emission.*

Downloaded from https://academic.oup.com/mnras/article-abstract/468/1/109/3038247 by inaf user on 13 July 2020

4.4 Lobe emission

For simplicity we take each lobe to be a sphere that is homogeneously filled with a magnetic field of corresponding coherence length $\lambda = 10$ kpc (e.g. Carilli & Taylor 2002; Celotti & Fabian 2004). The total injected power, $P_{\rm e,lobe}$, follows distribution given by equation (1), with different parameters from the jets and the hotspots. At variance with the hotspots, we assume that, within the lobes, the magnetic field energy is in equipartition with the electron energy, enabling us to infer the magnetic field value (unlike the hotspots, where the size sets the balance between magnetic and particle energy density, the lobe sizes are basically unconstrained, forcing us to assume equipartition to derive them in turn; this yields lobe sizes of the order of 50 kpc.[11]) For both systems, $B_{\rm lobe} < B_{\rm CMB}$ (equation 2), implying that the *synchrotron radio emission from the lobes is quenched, whereas X-ray emission by the inverse Compton scattering dominates the radiative power output*.

5 DISCUSSION AND CONCLUSIONS

In this work, we constructed and modelled the SEDs of two high-z ($z > 3.5$) radio galaxies to investigate the radiation mechanism of the extended emission in GHz radio and X-ray bands. One of our conclusions is that the synchrotron radio emission from the lobes is quenched by the CMB photons that are upscattered into the X-ray band. One of the key challenges faced by CMB quenching as a viable mechanism to account for the deficit of high redshift, radio-loud AGNs is provided by the fact that, for these systems, the measured $L_{\rm X}/L_{\rm radio}$ fails to increase with redshift as $(1 + z)^4$ over a fairly broad redshift range (Smail et al. 2012; Smail & Blundell 2013). As a possible explanation, these works suggest that *IR photons from the host galaxy* could provide a sizable – possibly dominant – fraction of the seed photons available for Comptonization into the X-ray band, thereby suppressing the strong redshift dependence that would be expected if CMB photons were solely responsible for seeding the IC process. If our modelling results are correct, however, this is unlikely to work above $z \simeq 2$. Specifically, the ratio between the IR and CMB photon energy densities depends on the system IR luminosity, $L_{\rm IR}$ and lobe size, d, as follows:

$$\frac{U_{\rm IR}}{U_{\rm CMB}} = \frac{L_{\rm IR}}{4\pi d^2 c U_{\rm CMB}} \sim 70\,\frac{L_{\rm IR,46}}{d^2_{10\,\rm kpc}(1+z)^4} \qquad (3)$$

Given the inferred values of d and $L_{\rm IR}$, the IR and CMB energy density contributions are still comparable at $z \sim 2$, above which $U_{\rm CMB}$ starts to prevail.

Furthermore, the main conclusion from our modelling is that the hotspots of 4C 41.17 and 4C 03.24 would be magnetically dominated. If so, independent from the ratio $U_{\rm IR}/U_{\rm CMB}$, most of the X-ray signal ought to be produced within the lobes, with only a negligible contribution from the hotspots. Conversely, any extended radio emission likely originates from the hotspots themselves, rather than the lobes. As a consequence, even though the *intrinsic* $L_{\rm X}/L_{\rm radio}$ *within the lobes should still increase as* $(1 + z)^4$, *the face-value, measured ratio, does not display any redshift dependence.*

In summary, although not aiming to completely solve the problem of missing high-redshift radio-loud AGNs, our work supports the viability of CMB quenching as an effective mechanism to significantly dim the diffuse radio emission from intrinsically jetted AGNs at high redshifts. For systems where the extended radio emission is dominated by the lobes instead of the hotspots, CMB quenching would cast them into the radio-quiet regime. However, while CMB quenching remains firmly in play for high-redshift radio galaxies, the limited sample under consideration in this work does not enable us to confirm to what extent this mechanism might be *entirely* sufficient to explain the apparent deficit of high-z radio-loud AGNs, or whether intrinsic obscuration of the central engine might be needed in addition (Ghisellini & Sbarrato 2016).

We close by acknowledging that the modelling of radio emission in this work – specifically the relative contribution of the lobes versus hotspots – has some level of degeneracy, in that the hotspots are not spatially resolved at these redshifts. Upcoming low-frequency radio observations (∼MHz), with the LOw Frequency Array (LOFAR; van Haarlem et al. 2013), should be able to isolate the contribution to the diffuse radio signal from the lobes alone Ghisellini et al. (2015).

[11] Notice that, while the parameters in Table 4 are given for a single lobe/hotspot, fluxes plotted in Figs 7 and 8 refer to the cumulative fluxes from each pair of lobes/hotspots.

ACKNOWLEDGEMENTS

GG and FT acknowledge contribution from grant PRIN–INAF–2014. This research has made use of the NASA/IPAC Extragalactic Database (NED) that is operated by the Jet Propulsion Laboratory, California Institute of Technology, under contract with the National Aeronautics and Space Administration.

REFERENCES

Ahn C. P. et al., 2012, ApJS, 203, 21
Ajello M. et al., 2009, ApJ, 699, 603
Arnaud K. A., 1996, in Jacoby G. H., Barnes J., eds, ASP Conf. Ser. Vol. 101, Astronomical Data Analysis Software and Systems V. Astron. Soc. Pac., San Francisco, p. 17
Becker R. H., White R. L., Helfand D. J., 1995, ApJ, 450, 559
Carilli C. L., Taylor G. B., 2002, ARA&A, 40, 319
Carilli C. L., Owen F. N., Harris D. E., 1994, AJ, 107, 480
Carter C., Karovska M., Jerius D., Glotfelty K., Beikman S., 2003, in Payne H. E., Jedrzejewski R. I., Hook R. N., eds, ASP Conf. Ser. Vol. 295, Astronomical Data Analysis Software and Systems XII. Astron. Soc. Pac., San Francisco, p. 477
Cash W., 1979, ApJ, 228, 939
Celotti A., Fabian A. C., 2004, MNRAS, 353, 523
Chambers K. C., Miley G. K., van Breugel W. J. M., 1990, ApJ, 363, 21
Cheung C. C., Stawarz Ł., Siemiginowska A., 2006, ApJ, 650, 679
Cheung C. C., Stawarz Ł., Siemiginowska A., Gobeille D., Wardle J. F. C., Harris D. E., Schwartz D. A., 2012, ApJ, 756, L20
Croston J. H., Hardcastle M. J., Harris D. E., Belsole E., Birkinshaw M., Worrall D. M., 2005, ApJ, 626, 733
Davis J. E. et al., 2012, Proc. SPIE, 8443, 84431A
Dickey J. M., Lockman F. J., 1990, ARA&A, 28, 215
Fabian A. C., Walker S. A., Celotti A., Ghisellini G., Mocz P., Blundell K. M., McMahon R. G., 2014, MNRAS, 442, L81
Francis P. J., Hewett P. C., Foltz C. B., Chaffee F. H., Weymann R. J., Morris S. L., 1991, ApJ, 373, 465
Freeman P., Doe S., Siemiginowska A., 2001, in Starck J.-L., Murtagh F. D., eds, Proc. SPIE Conf. Ser. Vol. 4477, Astronomical Data Analysis. SPIE, Bellingham, p. 76
Freeman P. E., Kashyap V., Rosner R., Lamb D. Q., 2002, ApJS, 138, 185
Garmire G. P., Bautz M. W., Ford P. G., Nousek J. A., Ricker G. R. Jr., 2003, in Truemper J. E., Tananbaum H. D., eds, Proc. SPIE Conf. Ser. Vol. 4851, X-Ray and Gamma-Ray Telescopes and Instruments for Astronomy. SPIE, Bellingham, p. 28
Gehrels N., 1986, ApJ, 303, 336
Georganopoulos M., Kazanas D., 2003, ApJ, 594, L27
Ghisellini G., Sbarrato T., 2016, MNRAS, 461, L21

Downloaded from https://academic.oup.com/mnras/article-abstract/468/1/109/3038247 by inaf user on 13 July 2020

Ghisellini G., Tavecchio F., Chiaberge M., 2005, A&A, 432, 401
Ghisellini G., Celotti A., Tavecchio F., Haardt F., Sbarrato T., 2014, MNRAS, 438, 2694
Ghisellini G., Haardt F., Ciardi B., Sbarrato T., Gallo E., Tavecchio F., Celotti A., 2015, MNRAS, 452, 3457
Haiman Z., Quataert E., Bower G. C., 2004, ApJ, 612, 698
Kratzer R. M., Richards G. T., 2015, AJ, 149, 61
Krimm H. A. et al., 2013, ApJS, 209, 14
Li J., Kastner J. H., Prigozhin G. Y., Schulz N. S., Feigelson E. D., Getman K. V., 2004, ApJ, 610, 1204
McGreer I. D., Helfand D. J., White R. L., 2009, AJ, 138, 1925
McKeough K. et al., 2016, ApJ, 833, 123
Mocz P., Fabian A. C., Blundell K. M., 2011, MNRAS, 413, 1107
Mocz P., Fabian A. C., Blundell K. M., 2013, MNRAS, 432, 3381
Morrison R., McCammon D., 1983, ApJ, 270, 119
Nousek J. A., Shue D. R., 1989, ApJ, 342, 1207
Roettgering H. J. A., van Ojik R., Miley G. K., Chambers K. C., van Breugel W. J. M., de Koff S., 1997, A&A, 326, 505
Sbarrato T., Ghisellini G., Nardini M., Tagliaferri G., Greiner J., Rau A., Schady P., 2013, MNRAS, 433, 2182
Sbarrato T., Ghisellini G., Tagliaferri G., Foschini L., Nardini M., Tavecchio F., Gehrels N., 2015, MNRAS, 446, 2483
Scharf C., Smail I., Ivison R., Bower R., van Breugel W., Reuland M., 2003, ApJ, 596, 105
Shakura N. I., Sunyaev R. A., 1973, A&A, 24, 337
Siemiginowska A., Smith R. K., Aldcroft T. L., Schwartz D. A., Paerels F., Petric A. O., 2003, ApJ, 598, L15
Skrutskie M. F. et al., 2006, AJ, 131, 1163
Smail I., Blundell K. M., 2013, MNRAS, 434, 3246
Smail I. et al., 2009, ApJ, 702, L114
Smail I., Blundell K. M., Lehmer B. D., Alexander D. M., 2012, ApJ, 760, 132
van Haarlem M. P. et al., 2013, A&A, 556, A2
van Ojik R., Roettgering H. J. A., Carilli C. L., Miley G. K., Bremer M. N., Macchetto F., 1996, A&A, 313, 25
Vanden Berk D. E. et al., 2001, AJ, 122, 549
Volonteri M., Haardt F., Ghisellini G., Della Ceca R., 2011, MNRAS, 416, 216
Wilson A. S., Young A. J., Shopbell P. L., 2000, ApJ, 544, L27
Wu J., Brandt W. N., Miller B. P., Garmire G. P., Schneider D. P., Vignali C., 2013, ApJ, 763, 109
York D. G. et al., 2000, AJ, 120, 1579
Yuan W., Fabian A. C., Worsley M. A., McMahon R. G., 2006, MNRAS, 368, 985

This paper has been typeset from a TEX/LATEX file prepared by the author.

Downloaded from https://academic.oup.com/mnras/article-abstract/468/1/109/3038247 by inaf user on 13 July 2020